5/18/00

SAND 2000-1450J

0-d energetics scaling models for Z-pinch-driven hohlraums

By M. E. CUNEO*, R. A. VESEY*, J. H. HAMMER**, J. L. PORTER, Jr.*

*Sandia National Laboratory, Albuquerque, NM, 87185-1193
** Livermore National Laboratory, Livermore, California, 94551

Wire array Z-pinches on the Z accelerator provide the most intense laboratory source of soft x-rays in the world. The unique combination of a highly-Planckian radiation source with high x-ray production efficiency (15% wall plug), large x-ray powers and energies (>150 TW, ≥1 MJ in 7 ns), large characteristic hohlraum volumes (0.5 to > 10 cm^3), and long pulse-lengths (5 to 20 ns) may make Z-pinches a good match to the requirements for driving high-yield scale ICF capsules with adequate radiation symmetry and margin. The Z-pinch driven hohlraum approach of Hammer and Porter [*Phys. Plasmas, 6, 2129(1999)*] may provide a conservative and robust solution to the requirements for high yield, and is currently being studied on the Z accelerator. This paper describes a multiple region, 0-d hohlraum energetics model for Z-pinch driven hohlraums in four configurations. We observe consistency between the models and the measured x-ray powers and hohlraum wall temperatures to within ±20% in flux, for the four configurations.

1. Introduction

Tungsten wire array [Sanford *et al.* 1996; Deeney *et al.* 1997] Z-pinches on the Z-driver [Spielman *et al.* 1998] have recently found many applications to driving high-temperature hohlraums [Matzen *et al.* 1997; Porter 1997; Leeper *et al.* 1999; Hammer *et al.* 1999; Nash *et al.* 1999; Olson *et al.* 1999; Sanford *et al.* 1999; Cuneo *et al.* 1999a, 1999b, 2000a; Slutz *et al.* 2000]. The unique combination of a highly-Planckian radiation source with high x-ray production efficiency (15% wall plug), large x-ray powers and energies (>150 TW, >1 MJ in 7 ns), large characteristic hohlraum volumes (0.5 to > 10 cm^3), and long pulse-lengths (5 to 20 ns) may make Z-pinches a good match to the requirements for driving high-yield scale ICF capsules with adequate radiation symmetry and margin. Assessment of Z-pinches for high-yield ICF is one of the goals of the research program at Sandia. Three different geometries are being studied to harness Z-pinches for indirect-drive ICF: the dynamic hohlraum [Nash *et al.* 1999; Slutz *et al.* 2000], static-wall hohlraum [Olson *et al.* 1999; Sanford *et al.* 1999], and Z-pinch driven hohlraum [Porter 1997; Hammer *et al.* 1999; Cuneo *et al.* 1999a, 1999b, 2000a]. Each of these approaches has a fundamentally different drive geometry, and hence different potential strengths and concerns, which have been previously described [Matzen *et al.* 1997; Leeper *et al.* 1999]. This paper describes 0-d hohlraum energetics models to relate x-ray power to hohlraum wall temperatures for four Z-pinch driven hohlraum configurations.

The Z-pinch Driven Hohlraum (ZPDH) concept is depicted in Fig. 1. In this concept, z-pinches are located in two primary radiation cavities or source hohlraums on either end of a secondary radiation cavity or capsule hohlraum. The majority of the secondary drive comes from re-radiation of the primary wall ($\geq$ 70 % of the flux, according to the models discussed below). Less than 30% of the secondary wall drive comes from direct-pinch illumination. This topology of coupling two hot x-ray source regions to a cooler ICF secondary is similar to some indirectly-driven laser hohlraum geometries [Lindl 1995; Rosen 1996]. Radiation flows into the secondary, through Be-spoke assemblies which are largely transparent to x-rays, and which also act to carry the Z-pinch current, as well as confine the Z-pinch plasma to the primary region. Experimentally, these Be spokes are observed to maintain their spoke-like character throughout the power pulse

[Hammer *et al.* 1999], offering the potential for high average transparency to x-rays in between the spoke material. These spokes impose a high-order azimuthal mode effect on radiation symmetry, that the capsule can tolerate [Hammer *et al.* 1999]. Future experiments will evaluate the degree of MHD-coupling of pinch plasma into the secondary, through the spokes. The Z-pinch implodes on additional foam cylinders (or wire arrays) to provide the radiation pulse shape required to maintain a capsule implosion on a low adiabat. The pulse-shaping concept has also been demonstrated experimentally, in principle [Hammer *et al.* 1999].

The Z-pinch-driven-hohlraum configuration theoretically provides the best capsule flux uniformity and smoothing over the mm-scale-length pinch spatial non-uniformities typical of Z-pinches [Hammer *et al.* 1999]. As noted, this concept provides two levels of radiation smoothing, e.g. primary and secondary hohlraum wall re-emission [Hammer *et al.* 1999; Vesey *et al.* 1998, 1999]. Secondary radiation symmetry of even modes (e.g. P2, P4, P6, etc.) is provided by altering the length and diameter of the secondary (and primary), as well as by varying the diameter and location of an axial shine shield, which prevents a pole-hot capsule drive [Vesey *et al.* 1998, 1999]. Fig. 1 shows a particular example with the secondary diameter the same as the wire array diameter. High-yield capsules of 5 mm diameter probably require a secondary diameter of 15 to 20 mm for adequate control of symmetry. The large hohlraum size may reduce sensitivity to wall motion. Symmetry can also be tuned by altering the shape of the secondary walls away from a purely cylindrical geometry with constrained flux optimization techniques [Vesey *et al.* 1998, 1999]. Radiation symmetry of odd modes (P1, P3, P5) is controlled by achieving adequate power balance and timing simultaneity for the 2-pinches [Hammer *et al.* 1999;

Vesey *et al.* 1998, 1999]. Coupling to higher order modes such as P3 and P5 appear to be tolerable. Control of P1 is the principal concern.

Experiments have shown that this scheme for coupling radiation to a secondary is practical and efficient [Cuneo *et al.* 1999a, 1999b, 2000a]. These results are being prepared for publication. Experiments are building in complexity towards the desired configuration in Fig. 1. Experiments have studied separately the energetics of Z-pinch driven primaries [Porter 1997] (Fig, 2), the energetics, average transparency of Be-spokes and radiation symmetry experiments in a primary-secondary configuration [Cuneo *et al.* 1999a, 1999b] (Fig. 3), and the power flow, pinch and hohlraum energetics, pinch power balance and simultaneity in a single-sided power feed, double-pinch driven secondary that can be fielded on Z [Cuneo *et al.* 2000a] (Fig. 4). This paper describes a 0-d hohlraum energetics model for the Z-pinch driven hohlraums in each of these four configurations, to look for consistency between measured x-ray powers and hohlraum wall temperatures. These models are similar in nature to those developed for laser hohlraums [Lindl 1995; Rosen 1996], and to earlier work on Z-pinch driven hohlraums [Hammer *et al.* 1999]. These models allow us to identify possible breakpoints in physics issues and driver performance, quickly evaluate experiments, and plan an organized research program. Based on these models, the energetics of the ZPDH appears to scale to the required high yield temperatures for a two-sided system at 60 MA/side (Fig. 1) if the x-ray power output of the pinch continues to scale with the square of the pinch current [Spielman *et al.* 1998]. Table I lists the key areas that are being studied to qualify this approach for high-yield fusion in our research program at Sandia.

2. Diagnostics

Hohlraum wall re-emission temperatures or pinch x-ray powers are measured by several different types of x-ray detectors through apertures in the hohlraum wall (XRD's [Chandler et al. 1999], ns-response Bolometers [Spielman et al. 1999], and Transmission Grating Spectrometers [Ruggles *et al.* 2000, Cuneo *et al.* 2000b]). The aperture size is measured with time-resolved, filtered x-ray framing cameras to correct both wall re-emission flux, and pinch x-ray flux for aperture closure [Chrien *et al.* 1999]. Initial aperture sizes of 12.6 to 16 mm^2 close by about 50% in primaries and about 35% in secondaries. Uncertainty of the wall re-emission flux and pinch x-ray measurements is ±20% in flux, (±5% in temperature), adding aperture closure and instrumental uncertainties in quadrature. This is comparable to temperature uncertainties for laser hohlraums [Lindl 1995]. Load currents are measured with B-dot loops [Stygar *et al.* 1997]

3. Models

In these 0-D models, we write coupled equations, which balance the power sources and sinks for each hohlraum in the system [Rosen 1995; Rosen 1996; Lindl 1995]. The power balance equations for each hohlraum (primary or secondary) have the form of power input = power loss.

3.1 Primary Only

The power balance equation is simple in the case of a single primary (Fig. 2):

$$P_p = \left[(1-\alpha_p)A_{wp} + A_{hp} + (1-\alpha_g)A_g\right]\sigma T_p^4 = \mathcal{A}_p\sigma T_p^4 \qquad (1)$$

where, α_p and α_g are albedos for the Au hohlraum wall, and the anode-cathode (AK) gap power feed respectively, and A_{wp}, A_{hp}, and A_g are the areas for the gold hohlraum wall, the diagnostic apertures, and the AK gap. The AK gap is a leak (like a diagnostic aperture) and is a main difference between Z-pinch-driven and laser-driven systems. Albedos are defined as $\alpha = P_{out}/P_{in}$ the ratio of reflected x-ray power to incident x-ray power [Rosen 1995]. Most of the "physics" for this model is contained in the proper choices for albedos. The effective albedos for the AK gaps are provided by 3-D viewfactor simulations [Vesey *et al.* 1998, 1999], allowing a calculation of the net x-ray return to the hohlraum from the transmission line feed. The main energy sink for hohlraums is the x-ray energy deposited in the Au wall that is not re-emitted. The incident x-rays drive a radiation heat-diffusion wave (a "Marshak wave") into the wall [Rosen 1995; Rosen 1996]. High-Z materials have a high reflectivity (≈ 0.8) to x-rays once they become hot, and the gradient driving energy into the wall flattens near the surface. The hohlraum Au wall albedos are a strong function of peak temperature, and temperature history or pulseshape. In previous work the wall loss (or equivalently wall albedo) was described by an analytic formulation [Rosen 1995; Rosen 1996; Lindl 1995], that was a good description of the physics for pulseshapes typical of laser hohlraums. In this work, the albedos are provided by 1-D radiation hydrodynamics (RMHD) calculations with the Lasnex code [Zimmerman and Kruer 1975] using the STA opacity tables.

An example radiation temperature pulseshape for a primary is shown in Fig. 5, with the corresponding calculated albedo history. The albedo is artificially clamped at 1 in these simulations. The hohlraum wall can become a net radiator, returning its energy to the system at some point as the input power falls, which would give an albedo greater than 1 by the above definition. The temperature history in Fig. 5 is representative of early (< 70 ns) [Chrien et al. 1999] and late time measurements (>70 ns) [Porter 1997]. The temperature up until 90 ns results from pinch radiation during its run-in or acceleration phase. This run-in radiation lowers the albedo (at peak) by pre-expanding the Au hohlraum wall. At 1.5 ns before peak run-in radiation increases the albedo slightly. However, the albedos near peak temperature are insensitive to the temperature history of the pinch run-in phase. No run-on radiation would give a change of < +3% in albedo. The inflection points in the albedo correspond to inflection points in the temperature history. In particular note that the albedo decreases at the transition point between the pinch-run in and the rapid temperature rise during the main x-ray pulse at pinch stagnation. The rapid increase in temperature increases the gradient driving energy into the wall for a short period lowering the albedo.

1- and 2-D RMHD simulations of Z-pinch driven hohlraums show a 1.5 ns timing delay between the peak pinch power and the peak temperature. In our 0-d treatment, we look for consistency between the peak pinch power, the temperature 1.5 ns before peak, with the albedo 1.5 ns prior to peak temperature. One might also look for consistency with the peak temperature (and albedo) with the pinch power 1.5 ns after peak pinch power. Experimentally we measure a timing delay between peak pinch and peak temperature of **2±1** ns. Fig. 6 plots the albedos 1.5 ns prior to peak temperature, and at peak temperature for the primary temperature pulseshape shown in Fig. 5, as the peak temperature is changed. Fig. 6 also plots similar albedos for a temperature pulse with a factor of 2x lower temperature during the run-in phase, showing the small change in albedo with changes in run-in temperature history.

The Z-pinch driven primary in Fig. 2 is a 24 mm diameter, 10 mm high cylindrical Au hohlraum (24x10 mm^2 notation), with an internal 300 wire, 11.5 μm tungsten wire array. This model shows good consistency between the experimentally measured peak pinch powers (145±26 TW, 4 shot average) and hohlraum radiation temperatures 1.5 ns prior to peak temperature (141±7 eV, 3 shot average), in Fig. 7. The peak radiation temperature is about 4% higher (147±7 eV). The temperatures are plotted as hundreds of eV, (i.e. 1 = 100 eV). This primary-only configuration will be used to study a number of issues listed in Table I such as: scaling of pinch x-ray output, scaling of radiation-driven, magnetically-tamped AK gap closure, pulseshaping performance, and pinch reproducibility which is related to pinch power balance in a double-sided system.

3.2 Primary/Secondary Configurations

In the case of configurations with one or two primaries and a secondary (Fig. 1, 3, 4), the description is more involved. The power balance for the primary (x-ray source chamber) is given by:

pinch power into primary - radiation transport to secondary =
wall loss in primary + loss out diagnostic apertures + loss out AK gap power feed(s)
+ loss into Be-spoke material

and for the secondary (x-ray sink or capsule chamber):

pinch power into secondary + radiation transport from primary =
wall loss in secondary + loss out diagnostic apertures + loss into Be-spoke material +
loss into capsule (if present)

These equations are given below. The power balance for each primary is (j = lower, upper):

$$f_p P_j - f_{ps} f_v A_{psj} \sigma\left(T_j^4 - T_s^4\right) = \mathcal{A}_{pj} \sigma T_j^4 \tag{2}$$

where f_p is the fraction of pinch power that remains in the primary, f_{ps} is the average transparency of the Be spokes, f_v is a filter transmission fraction, A_{psj} is the entrance area to the secondary, and the effective loss area for the primary $\mathcal{A}_{pj}$ is given by

$$\mathcal{A}_{pj} = \left[\left(1-\alpha_{pj}\right)A_{wj} + A_{hj} + \left(1-\alpha_g\right)A_g + \left(1-\alpha_{gu}\right)A_{gu} + \left(1-\alpha_{Be}\right)\left(1-f_{ps}\right)A_{psj}\right] \tag{3}$$

There are 2 new terms in Eq. 3 compared to Eq. 1: loss of radiation through an additional AK gap connecting lower and upper pinch (as in Fig. 4) and loss into Be spoke material. The terms included in Eq. 3 encompass four cases. There is no power feed connecting the bottom primary to upper primary (A_{gu}=0) in the case of a single primary (Fig. 2). In this case, A_{psj}=0, and f_p=1 recovering Eq. 1. For a single-sided secondary (Fig. 3), or a double-feed, double-pinch (Fig. 1), there is no power feed connecting to an upper pinch (A_{gu}=0). Finally, there is no standard AK gap power feed for the upper primary (A_g=0), for a single-feed, double-pinch case (Fig. 4). The lower primary has both gap loss terms in this case. The effective gap albedos near peak temperature α_g (=0.34) and α_{gu} (=0.40) are taken from viewfactor calculations [Vesey *et al.* 1998, 1999] and appear to be insensitive to the exact amount of gap closure.

Summing over all primaries j, the secondary power balance is given as:

$$\sum_j \left[f_s f_{ps} f_v P_j + f_{ps} f_v A_{ps} \sigma\left(T_j^4 - T_s^4\right)\right] = \mathcal{A}_s \sigma T_s^4 \tag{4a}$$

or, using $P_u = f_u P_l$

$$f_s f_{ps} f_v P_l (1 + f_u) + \sum_j f_{ps} f_v A_{ps} \sigma\left(T_j^4 - T_s^4\right) = \mathcal{A}_s \sigma T_s^4 \tag{4b}$$

where f_s is the fraction of pinch power that directly shines into the secondary, f_u is the ratio of the upper pinch to lower pinch power, and the effective loss area for the secondary $\mathcal{A}_s$ is given by

$$\mathcal{A}_s = \left[(1-\alpha_s)A_{ws} + A_{hs} + (1-\alpha_{Be})(1-f_{ps})\sum_j A_{psj} + (1-\alpha_c)A_c\right] \quad (5)$$

The direct shine fraction f_s is also calculated with a viewfactor treatment [Vesey *et al.* 1998, 1999]. These calculations give a range of 5% to 16% for various shine shield, secondary, and pinch diameters, and pinch x-ray angular distributions, and is reduced for larger shields, smaller secondaries, and for non-Lambertian pinch x-ray emission. AK gap closure by the Au hohlraum wall material would make the hohlraum a better radiation trap. The size of this gap near peak temperature is unknown and remains an additional uncertainty in the modeling. 2-D RMHD hohlraum simulations [Hammer *et al.* 1999] indicate about 1.5 mm expansion of the Au wall into the 2 mm gap at peak temperature. 2-D RMHD simulations of pinches have suggested that there may be some current loss at this AK gap based on comparison to measured x-ray powers and current pulseshapes [Peterson et al. 1999]. These 2 or 3 coupled equations are solved for the primary and secondary temperatures T_{pj} and T_s, with temperature varying gold wall albedos, by an iterative scheme, which converges quickly. Table II summarizes the parameters used in the equations.

The main power source is the pinch power in the primary (P_p). Coupling to the secondary is described by a direct pinch shine fraction ($f_s f_{ps} P_p$) and a cavity coupling ($f_{ps}A_{ps}(T_p^4-T_s^4)$) , both terms modified with an average spoke transparency f_{ps}. The radiation coupling from primary to secondary is given by $T_p^4-T_s^4$ rather than as $\alpha_p T_p^4-T_s^4$. In the latter case, the first term is the wall re-emission power in the primary ($\alpha_p T_p^4$), rather than the total radiation field (T_p^4, which includes pinch power). This is probably a more appropriate treatment in the case where the direct shine is included separately as in the above equations. However, T_p^4-T_s^4 provides a closer match between 2-D RMHD and viewfactor codes which show that 70% of the power transfer to the secondary is from the cavity coupling ($f_{ps}A_{ps}(T_p^4-T_s^4)$) while 30% results from direct pinch shine ($f_s f_{ps} P_p$). The use of $\alpha_p T_p^4$-T_s^4 gives closer to a 60% cavity coupling/40% direct shine split. The use of T_p^4-T_s^4 may provide a closer approximation to the actual radiation transfer to the secondary since 90% of the pinch power remains in the primary. This term might also compensate for temperature gradients in the primary (increasing temperature away from the AK gap) which increases power transfer to the secondary.

3.3 Example calculations for single-sided secondary configuration

In the case of a single-sided secondary, Eqs. 2 through 5 allow the pinch power and spoke transparency to be treated as two unknowns, and determined from simultaneous measurements of primary and secondary radiation temperature. To illustrate this, we solve Eqs. 2 through 5 for f_{ps}, neglecting the Be-loss terms (depending on f_{ps}) within A_p and A_s. The result in Eq. 6, depends approximately linearly on $\xi = \alpha_s T_s^4/\alpha_p T_p^4$, the ratio of the wall re-emission flux in the secondary to the wall re-remission flux in the primary.

$$\mathrm{f}_{ps} = \frac{\frac{\alpha_p}{\alpha_s} A_s}{\mathrm{f}_s \mathrm{f}_v \left[A_p + \frac{\alpha_p}{\alpha_s} A_s \xi \right] + \mathrm{f}_v \mathrm{A}_{ps} \left[1 - \frac{\alpha_p}{\alpha_s} \xi \right]} \xi \qquad (6)$$

Experiments can determine both $\alpha_s T_s^4$ and $\alpha_p T_p^4$ independently, with two, cross-calibrated wall re-emission measurements. ξ can be experimentally determined within ±10% by a relative calibration of two sets of instruments. There is a weak dependence of Eq. 6 on the temperature (and therefore pinch power) through albedos α_s and α_p, and the effective wall areas A_p and A_s which contain albedos. Eq. 6 is presented primarily to motivate the linear scaling with ξ. Model calculations of the Be spoke transparency f_{ps}, including the Be-loss and the variation of albedo with temperature are shown in Fig. 8 for a range of pinch powers (130±23 TW), and a range of direct shine fractions (5-16%) indicating small deviations from linear behavior. Fig. 8 shows the insensitivity to the absolute value of the pinch power, which makes this a feasible indirect inference of f_{ps}. Data for the ratio of secondary to primary wall re-emission powers from one experiment ($\xi = (91.8/117.8)^4 = 0.369 \pm 0.04$) is plotted on Fig. 8 indicating an average spoke transparency of 68±7%. Physically, Eq. 6 is linear because T_s^4 scales linearly with f_{ps} (Eqs. 2, 4), and the variation in T_p is very flat with f_{ps} (see Fig. 9). There is a strong dependence of f_{ps} on the direct shine fraction f_s as shown in Fig. 8, which indicates the importance of including this effect for an inference of transparency. Without direct shine, the inferred spoke transparency could increase by up to 30%. The entrance area coupling primary to secondary, A_{ps}, is reduced in the experiments from the initial area by the expansion of the Au hohlraum walls (0.3 to 0.5 mm from 1-D RMHD simulations). Accounting for the reduction of A_{ps} in the model increases the net transparency of the Be spokes by about 10%.

Eq. 2 and 4 can be added to obtain the pinch power as

$$P_p = \left[\mathcal{A}_p + \frac{\alpha_p}{\alpha_s} \mathcal{A}_s \xi \right] \sigma T_p^4 \qquad (7)$$

using $f_p + f_s f_v f_{ps} = 1$ from conservation of energy. Eq. 7 shows that the pinch power is a weak function of the secondary temperature through the albedo's and ξ. Fig. 9 plots the primary and secondary radiation temperatures versus Be transparency fraction f_{ps} , for a range of pinch powers, and compares them with experimental data. The data are plotted at the transparency independently determined from the analysis in Fig. 8. These data are consistent with a pinch power of 130±23 TW on this particular shot.

Fig. 10 shows the power scaling of hohlraum temperature for the single-sided secondary configuration. This model shows good consistency between the experimentally measured peak pinch powers (145±26 TW, 4 shot average) and the primary (124±6 eV) and secondary hohlraum radiation temperatures (98±5 eV), 1.5 ns prior to peak temperature. The peak temperatures are about 2 to 3% higher than this curve. This data is the same shot analyzed in Fig. 8 and 9, for which a pinch power of 130±23 TW was inferred from the temperatures, within the statistical variation of the measured pinch powers. This may explain the 3 eV discrepancy between the primary data and the model. Lowering the data points to a 130 TW power, moves them onto the model curve. This primary-secondary configuration can be used to study the scaling of Be spoke transparency with pinch mass, and hohlraum temperatures, and to study MHD coupling to the secondary.

3.3 Double-sided secondary configurations

This model is applied to a single-sided power feed, double-sided secondary configuration in Fig. 11. Good agreement is observed with the primary (94±4 eV) and secondary (82±3 eV) radiation temperatures 1.5 ns prior to peak temperature at the observed total pinch power of 115±20 TW. Greater load inductance in this configuration resulted in lower total load current and pinch power. This configuration can be used to study pinch power balance, simultaneity, and radiation symmetry, and possibly perform capsule implosions, prior to the development of a machine architecture compatible with a two-sided power feed [Struve *et al.* 1999]. This configuration does not scale to meet high-yield requirements of 220 eV in the secondary at 60 MA/side [Hammer *et al.* 1999].

Application of this model to multiple primary systems requires at least one additional measurement, and additional assumptions. There are 3 equations and 7 unknowns. The 7 unknowns are 3 temperatures, 2 pinch powers, and 2 spoke transparencies. For example, we can measure the temperature of both primaries and the secondary (e.g. T_{pu}, T_{pl}, and T_s), and then solve for the pinch powers P_{pu}, P_{pl}, and the effective or average transparency of both spokes $<f_{ps}>=(f_{pu}+f_{pl})/2$. It is also possible to measure T_{pl}, T_s, and the ratio of peak pinch powers $f_u = P_{pu}/P_{pl}$ and infer the pinch powers P_{pu}, P_{pl} and the average transparency $<f_{ps}>$. Finally, we could also measure T_{pu}, T_{pl}, and T_s and $f_u = P_{pu}/P_{pl}$, and infer P_{pu}, P_{pl} and separate transparencies for both upper and lower spokes.

Fig. 12 gives results for the high-yield configuration of Fig. 1, indicating good agreement between the model and scaled-Z data. The single-sided Z secondary data from Fig. 9 is scaled up by $2^{1/4}$ to 117±6 eV to account for the temperature increase from an additional primary. The experimentally demonstrated Z hohlraum energetics scales [Cuneo *et al.* 1999a; 1999b] to the high-yield requirements of a 220 eV peak secondary wall re-emission temperature at a pinch power per side of 1400 TW, for a Au hohlraum wall. This corresponds to a pinch current of 59 MA/side, if the pinch x-ray power continues to scale with the square of the pinch current. The use of Au-Gd hohlraum cocktail walls [Orzechowski *et al.* 1996; Hammer et al. 1999] would lower the pinch requirements or further increase the secondary temperatures.

4.0 Conclusions

These 0-d models show good agreement with the measured pinch x-ray powers and hohlraum wall temperatures to within ±20% in flux (±5% in temperature) accounting for aperture closure and instrumental uncertainties. Issues such as partial AK gap closure, and non-Lambertian pinch emission affect the agreement to about the ±15% level in flux, within this uncertainty, hence we cannot conclude anything about these issues from this model. This level of flux uncertainty is typical for measurements of wall re-emission, and pinch powers. Improvements in temperature accuracy or additional measurements of AK gap closure or pinch angular emission profile are necessary to improve energetics assessment beyond the ±20% level.

There are other issues which could affect the scaling of hohlraum temperatures upwards with higher current Z-pinch drivers as shown in Figs. 7, 10, 11, 12. For example, the Z-pinch mass must increase with the square of the pinch current for a constant implosion time. Hence a pinch at 60 MA must have more than 9 times the mass as at 20 MA. The increasing pinch opacity [Hammer *et al.* 1999] may decrease the x-ray output below the scaling with square of the driver current that has been established on drivers at the 2 to 20 MA level [Spielman *et al.* 1998]. A simple scaling argument for the level of pinch current and mass where tungsten pinch opacity effects will start to limit x-ray power in given in appendix A. The electromagnetic power that supplies the pinch is delivered through a 2-3 mm AK gap at the base of the pinch. This gap is subjected to radiation fields of 250 eV in the primary (Fig. 12), at peak magnetic fields of more than 1000 T in the high yield scale system at 60 MA. A simple analytic scaling for magnetically-tamped, radiation-driven AK gap closure is given in appendix B to provide some guidance on this issue.

These and the other issues listed in Table I are part of our ongoing high-yield assessment for Z-pinches.

Acknowledgements

We gratefully acknowledge the experimental efforts of the Z operations teams led by J. Seamen, including the wire array lab (T. L. Gilliland, P. G. Reynolds), target development lab (D. Hebron, S. Dropinski, R. Hawn), and materials processing and coating lab (J. McKenney). We also thank the following for development, calibration and fielding of various diagnostics: L. E. Ruggles, W. W. Simpson, H. Seamen, P. Primm for the transmission grating spectrometers, G. Chandler, J. Torres, and J. McGurn, for XRD's and bolometers, and T. Wagoner and W. A. Stygar, for B-dot loop current measurements. We thank W. W. Simpson for the preparation of the 3-D hohlraum figures. We acknowledge helpful conversations with R. B. Spielman and R. E. Chrien. We thank

M. K. Matzen and J. P. Quintenz for programmatic support. Sandia is a multi-program laboratory operated by Sandia Corporation, a Lockheed Martin Company, for the U. S. Department of Energy under Contract No. DE-AC04-94AL85000.

Appendix A. Scaling of Pinch X-ray Output with Pinch Mass and Current

We will assume the pinch is a static, uniform density, uniform cylinder of hot W, with a temperature profile obtained from a solution to the radiation heat diffusion equation. We assume that the total energy (kinetic + magnetic [Peterson *et al.* 1998]) available to the Z-pinch scales with the square of the pinch current. This energy is partitioned between radiated energy and internal energy tied up in the specific heat of the material:

$$E_{tot} = E_{rad} + E_{int} \tag{A1}$$

The second term becomes increasingly important as the pinch mass and opacity increases. We use a normalization from experiments on Z where the effective energy in the 7 ns fwhm pinch power pulse is 1 MJ at 19 MA load current. The results of this appendix give an internal energy of 0.25 MJ at 19 MA, hence we assume:

$$E_{tot} = 1.25\left(\frac{I}{19}\right)^2 \text{ MJ} \tag{A2}$$

The internal energy is given by

$$E_{int} = m_p h = 4.2\pi r_s^2 l_p \rho^{0.86} T_{heV}^{1.6} \text{ MJ} \tag{A3}$$

where m_p, r_s, l_p, and ρ are the mass, radius length and density of the pinch at stagnation, and T is the pinch temperature in hundreds of eV. We assume here that the W pinch plasma specific heat can be approximated by an expression for the specific heat of Au given in [Lindl 1995]. In order that the implosion time remain constant as the current is increased, the 6 mg mass used on the Z arrays must increase with the square of the current

$$m_p = 6\left(\frac{I}{19}\right)^2 \text{ mg} \tag{A4}$$

The radiated energy is simply:

$$E_{rad} = \sigma T_s^4 A_s t_p = 0.01028 A_s T_s^4 t_p \text{ MJ} \tag{A5}$$

where A_s., and T_s are the pinch surface area and surface temperature respectively in cm^2 and heV, and t_p is the pinch power pulse fwhm in ns. The optical depth of the W pinch plasma is

$$\tau = K_R \rho r_s = 6x10^3 K_o \rho^{1.3} T_{heV}^{-1.5} r_s \tag{A6}$$

where we again assume the the W plasma Rosseland opacity can be approximated by an expression for Au given in [Lindl 1995]. Finally for a steady-state pinch system the core temperature (T_c) and surface temperature (T_s) are related by

$$T_c = T_s \tau^{0.25} \tag{A7}$$

A solution of 1-D radiation heat diffusion equation provides a temperature profile across a pinch, assumed to have a uniform mass density:

$$T(r) = T_c\left(1 - f\frac{r^2}{r_s^2}\right)^{\frac{1}{4(\lambda+1)}} \tag{A8}$$

where f is a small correction given by

$$f = 1 - \left(\frac{4}{3(\lambda+1)\tau_c}\right)^{\lambda+1} \tag{A9}$$

where $\lambda = 1.5/4 = 0.375$ and τ_c is the opacity evaluated at the core temperature with the full pinch radius. Note that for high optical depth systems, f is near 1, i.e. for $\tau = 10$, $f = 0.96$. We integrate the specific heat (h in Eq. A3) across the temperature profile in A8 to obtain a correction factor for internal energy. This factor is:

$$g=\left[\frac{1}{\left(\frac{\gamma}{\lambda+1}+1\right)f}\right]\left[1-(1-f)^{\left(\frac{\gamma}{\lambda+1}+1\right)}\right] \qquad \text{(A10)}$$

where $\gamma=1.6/4=0.4$. This correction factor g is near 0.77 above about 10 MA.

Equations A1 through A10 can be iterated to find a self-consistent combination of E_{rad}, E_{int}, T_c, T_s, τ. The effective optical depth and specific heat are dominated by the core temperature. These results are plotted in Fig. 13 for a case with r_s = 0.1 cm, and l_p = 1.0 cm. We find that the internal energy scales as $I^{2.8}$ while the radiated energy scales as $I^{1.7}$ over the range of 10 to 60 MA. The optical depth of the core scales as $I^{1.4}$ from about 9.2 at 19 MA, to 50 at 60 MA. Over the range of 10 to 35 MA, the radiated energy scales as $I^{1.8}$. Note that an increasingly larger fraction of the total energy goes into specific heat as the pinch mass and opacity increase. At 60 MA about half of the energy goes into radiation (6.3 MJ) and half into specific heat (6.2 MJ). X-ray bolometers on Z can currently measure energy to about ±10% in absolute magnitude [Spielman *et al.* 1999], and systematic relative differences between different configurations can be confirmed reliably with multiple samples. This suggests that careful experiments which vary the pinch mass, at fixed implosion time and current, or vary the pinch current at fixed implosion time might be able to discern the increase of the internal energy with increasing mass and current. The predicted internal energy at 28 MA is almost 0.7 MJ. This deficit might be easily discernable.

There are or course several caveats for this simple estimate. The internal energy is underestimated since the time-dependence has been neglected. However, the Rayleigh-Taylor

(RT) instability will break up the plasma, possibly resulting in a lower effective opacity, and hence lower internal energy. Turbulent mixing of the core and outer layers could also bring hot material to the surface and increase radiation power [Hammer *et al.* 1999]. The Rayleigh-Taylor (RT) instability growth is expected to dominate the pinch fwhm on Z [Spielman *et al.* 1998] based on 2-D RMHD simulations [Hammer *et al.* 1999; Peterson *et al.* 1998, 1999]. The linear growth time for RT scales with $(\text{acceleration})^{0.5}$*time, hence a system with a fixed size, force/mass and implosion time might be expected to have the same pinch fwhm. This implies a x-ray power of 900 TW at 60 MA with 6.3 MJ radiated, somewhat below what is required for high-yield. 2-D RMHD simulations of a 60 MA W pinch with this radii and mass show about 1000 TW [Peterson, private communication]. Low Z pinch materials were used in [Hammer et al. 1999] to decrease the optical depth and increase radiated power to 1200-1400 TW at 60 MA.

Appendix B. Scaling Radiation Ablation and Magnetic Tamping Pressures

The size of the anode-cathode (AK) gap power feed near peak temperature is unknown and remains an uncertainty in our modeling of the energetics. AK gaps have been operated as small as 1.5 mm on the Z accelerator at 19 MA peak current on a 1 cm radius [Porter 1997]. An important question is how this AK gap performance will scale at higher hohlraum temperatures (250 eV) and higher magnetic fields (1200 T at 60 MA and 1 cm radius). As noted above, 2-D RMHD simulations of hohlraums [Hammer *et al.* 1999] and pinches [Peterson *et al.* 1999] directly or indirectly show some closure of this AK gap. AK gap closure by the Au hohlraum wall material would make the hohlraum a better radiation trap. Closure of the AK gap however, could decrease the pinch x-ray output by shorting the input current. Further experiments are required to elucidate this balance, and its scaling with gap, hohlraum temperature and current. This appendix provides a simple comparison of radiation ablation pressure to magnetic pressure as a first step to understanding the behavior of these small, highly-driven gaps.

The radiation ablation pressure can be calculated by equating the incident radiation flux intensity to the hydrodynamic power [Lindl 1995]:

$$I = \sigma T^4 = \frac{dm}{dt} C_s^2 = \frac{5}{2} P_a C_s \text{ Watts/cm2} \qquad \text{(B1)}$$

where T is the radiation temperature of the incident radiation, dm/dt is the mass ablation rate per unit area from the surface, C_s is the isothermal sound speed $=0.976(ZT/\mu)^{1/2}$ cm/μs for T in eV, and P_a is the radiation ablation pressure on the surface. In the case of a low Z material with low opacity (high transparency to incident radiation) we find:

$$P_{a(low\_Z)} = 5.7 T_{heV}^{3.5} \text{ Mbar} \qquad \text{(B2)}$$

where T is in hundreds of eV, and where the low Z material is assumed fully stripped ($Z/\mu=1/2$). This is high compared to [Lindl, 1995] who reports $P_{a(low\_Z)} = 3T^{3.5}$ Mbar and compared to RMHD simulations which find closer to $P_{a(low\_Z)} = 4T^{3.5}$ Mbar. We will use the numerical coefficient of this last result. The result in B2 can be scaled to account for the decrease in expansion velocity and increase in x-ray reflectivity of the high-Z wall material which will lower the ablation pressure compared to the scaling in B2:

$$P_{a(high\_Z)} = \frac{C_{s(low\_Z)}}{C_{s(high\_Z)}} (1-\alpha) P_{a(low\_Z)} \qquad \text{(B3)}$$

The ratio of sound speeds is

$$\frac{C_{s(low\_Z)}}{C_{s(high\_Z)}} = 2.1T_{heV}^{-0.225} \tag{B4}$$

for T in hundreds of eV, using a result for the average ionization state of Au as a function of temperature from [Lindl 1995]:

$$\bar{Z} = 23T_{heV}^{0.45} \tag{B5}$$

The wall loss fraction (1-α) is given by [Lindl 1995]

$$(1-\alpha) = \frac{0.32}{T_{heV}^{0.7}\tau_{ns}^{0.38}} \tag{B6}$$

where T is in hundreds of eV, and τ is the radiation pulsewidth in ns. Note that for small τ, the albedo is lower, and the effective ablation pressure is higher (see Eq. B7). The effective τ for Z parameters at peak temperature based on the 1-D RMHD calculations reported above (Fig. 6) is about 9.4 ns giving the calculated albedo of 0.88 at 140 eV. Substituting B6 and B4 into B3 and using the scaling of 4 Mbar ablation pressure for a low-Z material at 100 eV (rather than 5.7 Mbar) we find:

$$P_{a(high\_Z)} = \frac{2.6T_{heV}^{2.6}}{\tau_{ns}^{0.38}} \text{ Mbar} \tag{B7}$$

The magnetic pressure is given by

$$P_m = \frac{B^2}{8\pi} = 1.57x10^{-3}\frac{I_{MA}^2}{r_{cm}^2} \text{ Mbar} \tag{B8}$$

where I is the load current in MA and r is the radius of the AK gap in cm. We can relate the I^2 scaling of magnetic pressure to the hohlraum temperature

$$E_{x-ray} \propto P_{x-ray} \propto I^2 \propto T^{3.6} . \tag{B9}$$

where the output x-ray energy and power of the pinch are assumed to be proportional to the square of the current, which is subsequently proportional to the scaling of the wall loss energy of the hohlraum with temperature from the above power balance work. Substituting B7, B8, and B9 into the ratio of magnetic to radiation ablation pressure we find:

$$\frac{P_m}{P_a} \propto \frac{B^2}{T^{2.6}} \propto \frac{I^2}{I^{1.44}} \propto \frac{T^{3.6}}{T^{2.6}} \propto I^{0.56} \propto T \qquad \text{(B10)}$$

which implies that the magnetic tamping scales upwards faster than the radiation ablation pressure. A well-behaved AK gap on Z may imply a well-behaved AK gap on higher current drivers.

It must also be noted that both the temperature and current vary as a function of time. Fig. 14 plots the magnetic pressure and radiation ablation pressure as a function of time for both Z parameters (20 MA peak load current, >140 eV peak radiation temperature) and parameters relevant to a high yield facility (60 MA peak load current, 250 eV peak radiation temperature). The temperature history uses the shape in Fig. 5, which is representative of early (< 70 ns) [Chrien et al. 1999] and late time measurements (>70 ns) [Porter 1997]. The magnetic pressure is calculated from a measurement of load current [Stygar *et al.* 1997]. The magnetic pressure exceeds the radiation ablation pressure by a factor of 2 to 5 during the first 90 ns of the implosion. This may explain why these small gaps are able to deliver current during the 100 ns pinch implosion time. The radiation pressure exceeds magnetic about 6 ns before the pinch stagnation for the Z parameters and 5 ns before for the high-yield parameters. Fig. 15 plots the ratio of magnetic to radiation ablation pressure (P_m/P_a) for both Z and high-yield conditions. P_m/P_a is increased during the pinch run-in phase, and the peak magnetic pressure is a larger fraction of the peak radiation pressure for the high yield case, in agreement with the scaling in Eq. B10.

The temperature increases from 70 to 140 eV (for Z) in 6 ns following the time that the ablation pressure exceeds the magnetic pressure. Assume that the Au wall will expand at the following rate during this period [Lindl 1995]:

$$C_s = 3T_{heV}^{0.8}\rho_{g/cm^3}^{-0.07}\ \mathrm{cm/\mu sec} \qquad \text{(B11)}$$

where ρ is the Au mass density in g/cm^3. An ion density of $2\text{x}10^{17}$ to $5\text{x}10^{19}$ cm^{-3} is sufficient to carry 1-10 MA for 10 ns and short the AK gap. This occurs at a Au atom density of $7\text{x}10^{15}$ to $3\text{x}10^{18}$ cm^{-3} ($\overline{Z}$=20 to 27 at 70 to 140 eV from Eq. B5 [Lindl, 1995]) which is a Au mass density of $2.4\text{x}10^{-6}$ to $8.5\text{x}10^{-4}$ g/cm^3. Eq. B11 then implies a Au material velocity of 3.7 to 9.7 cm/μsec from both anode and cathode sides of the AK gap at this range of densities. A 2 mm gap shorts electrically in 10 to 30 ns at these velocities. Assuming a length of the feed region of 0.1 to 0.5 cm, a Au mass density of $\rho = 1.4\text{x}10^{-3}$ to $1.08\text{x}10^{-2}$ g/cm^3 is sufficient to provide an optical depth of 1 for outgoing hohlraum radiation (at 70 to 140 eV) [see Eq A6, Lindl 1995]. The velocity of this surface is about 3.0 to 6.2 cm/μsec, blocking all radiation from a 2 mm gap within about 15 to 30 ns. The AK gap would close by 0.9 ± 0.3 mm within 10 ns at these velocities. Fig. 14 shows that although the magnetic pressure exceeds the ablation pressure for a somewhat longer period at high yield conditions (1ns), the velocity of the Au will be 50% faster at the higher temperatures (Eq. B11).

This simple scaling gives increased confidence in our ability to scale this system to levels relevant for high-yield. More work must be done to characterize the behavior of this gap.

Additional physics that may play a role are electron-driven expansion of material from the wall, cross-field motion of charged particles by kinetic effects, the balance of plasma erosion by current flow and resupply from wall ablation, cross-field motion of plasma by other instabilities, and *JxB* acceleration in the axial direction (self-clearing) of plasma material out of the gap.

REFERENCES

CHANDLER, G. A. *et al.* 1999 *Rev. Sci. Inst.*, **70**, 561.

CHRIEN, R. E. *et al.* 1999 *Rev. Sci. Inst.*, **70**, 557.

CUNEO, M. E. *et al.* 1999a *26th IEEE Conf. on Plasma Sci.*

CUNEO, M. E. *et al.* 1999b *Bull. Amer. Phys. Soc.*, **44**, 40.

CUNEO, M. E. *et al.* 2000a *27th IEEE Conf. on Plasma Sci.*

CUNEO, M. E. *et al.* 2000b in *Proceedings of the 13th Conf. On High Temp. Plasma Diag.*. Tucson, AZ, to be published.

DEENEY, C. *et al.* 1997 Phys. Rev. E, **56**, 5945.

HAMMER, J. H. *et al.* 1999 *Phys. Plasmas*, **6**, 2129.

LEEPER, R. J. *et al.* 1999 *Nuclear Fusion*, **39**, 1283.

LINDL, J. D. 1995 *Phys. Plasmas*, **2**, 3933.

MATZEN, M. K. *et al.* 1999 *Plasma Phys. Control. Fusion*, **41**, A175.

NASH, T. J. *et al.* 1999 *Phys. Plasmas*, **6**, 2023.

OLSON, R. E. *et al.* 1999 *Fusion Technology*, **35**, 260.

ORZECHOWSKI, T. J. *et al.* 1996 *Phys. Rev. Lett.*, **77**, 3545.

PETERSON, D. L. *et al.* 1998, Phys. Plasmas, 5, 3302.

PETERSON, D. L. *et al.* 1999, *Phys. Plasmas*, **6**, 2178.

PORTER, J. L., Jr. 1997 *Bull. Amer. Phys. Soc.*, **42**, 1948.

ROSEN, M. D. 1995 Lawrence Livermore National Laboratory, Livermore, CA, *UCRL-JC-121585* (unpublished).

ROSEN, M. D. 1996 *Phys. Plasmas*, **3**, 1803.

RUGGLES, L. E. *et al.* 2000 in *Proceedings of the 13th Conf. On High Temp. Plasma Diag.*. Tucson, AZ, to be published.

SANFORD, T. W. L. *et al.* 1996 *Phys. Rev. Lett.*, **77**, 5063.

SANFORD, T. W. L. *et al.* 1999 *Phys. Rev. Lett.*, **83**, 5511.

SPIELMAN, R. B. *et al.* 1998 *Phys. Plasmas*, **5**, 2105.

SPIELMAN, R. B. *et al.* 1999 *Rev. Sci. Inst.*, **70**, 651.

STYGAR, W. A. *et al.*, 1997 in *Proceedings of the Inter. Pulsed Power Conf.*, Baltimore, MD, G. Cooperstein and I. Vitkovitsky, Eds., **2**, 1258, IEEE Cat. No. 97CH36127.

STRUVE, K. W. *et al.* 1999 in *Proceedings of the Inter. Pulsed Power Conf.*, Monterey, CA, to be published.

SLUTZ, S. A. *et al.* 2000 *submitted to Phys. Plasmas.*

VESEY, R. A. *et al.* 1998 *Bull. Amer. Phys. Soc.*, **43**, 1903. The Lightscape visualization system is a product of Lightscape Technologies.

VESEY, R A. *et al.* 1999 *Bull. Amer. Phys. Soc.*, **44**, 227.

ZIMMERMAN, G.B., and KRUER, W.L, 1975 *Comments Plasma Phys. Control. Fusion*, **2**, 51.

Figure Captions

Figure 1. High yield Z-pinch driven hohlraum configuration i.e. a double-sided power feed, double-sided secondary showing: a) two 24x10 mm^2 primaries or x-ray source hohlraums with 300, 11.5 μm W wire arrays, b) 20x15 mm^2 secondary with 5 mm diam. high yield capsule, c) two Be spoke assemblies, d) two foam pulse shaping cylinders on axis in the primaries, and e) two 5 mm diam. axial shine shields. These Z-pinch primaries are each driven by a separate set of transmission lines. Current smoothing between these lines is performed in the output section of the accelerator over a large number of individual accelerator modules to provide identical current pulses to the two pinches [Struve *et al.* 1999].

Figure 2. 24 x 10 mm^2 Z-pinch driven primary hohlraum configuration. This configuration smooths the pinch radiation and provides a large surface area to drive 3 to 12 side-viewing experimental packages with very similar radiation histories [Porter 1997]. This primary is also used to drive large diameter secondaries for the high-yield ICF concept. This configuration can be used to study pinch energetics and power flow physics.

Figure 3. Z-pinch driven single-sided secondary hohlraum configuration. A 24x10 mm^2 primary drives a 17x15 mm^2 secondary through a 17 mm diam. Be spoke assembly, providing a simple testbed for measuring spoke transparency, radiation coupling, and MHD isolation from the primary.

Figure 4. Single-sided power feed, double-sided secondary hohlraum configuration used to perform radiation symmetry, pinch power balance and simultaneity assessment on the Z accelerator, prior to the availability of an accelerator configuration with a two-side power feed. The secondary is suspended off of the tungsten wires and becomes part of the power feed to supply the upper pinch.

Figure 5. Example primary temperature pulse (solid line) and calculated Au wall albedo history (dotted line) derived from 1-D RMHD simulations using STA material opacities.

Figure 6. Calculated albedos versus peak temperatures: at peak temperature (solid circles/solid lines) and 1.5 ns prior to peak temperature (solid circles/dotted lines), for primary temperature pulses, and pulses with about a factor of 2 lower run-in temperature (open circles).

Figure 7. Comparison of 0-d temperature scaling model for the primary radiation temperature (1.5 ns prior to peak temperature) (Fig. 2) compared with measured primary temperature and pinch power, with the AK gap fully open.

Figure 8. Calculated Be spoke transparency f_{ps} versus the ratio of secondary to primary wall re-emission powers, $\xi = \alpha_s T_s^4/\alpha_p T_p^4$, for a single-sided secondary temperature configuration (Fig. 3). These are shown for a range of pinch powers (130±23 TW, light broken lines with circular symbols), and for a range of direct shine fractions (5% to 16%, heavy dotted lines with circular symbols). The inferred transparnecy is insensitive to the range of pinch powers. A ±10% uncertainty in transparency results from the range in direct shine fractions.

Figure 9. Primary and secondary temperatures versus Be spoke transparency f_{ps} for a single-sided secondary temperature configuration (Fig. 3). These curves are calculated for $P_p = 130\pm23$ TW, and for f_s=0.10 with a secondary entrance and AK gap fully open.

Figure 10. Comparison of 0-d temperature scaling model for single-sided secondary configuration (Fig. 3) with the measured primary (circle) and secondary (square) radiation temperatures and pinch powers. These curves are calculated for $f_{ps} = 0.63$, and $f_s = 0.10$, with the secondary entrance and AK gaps fully open.

Figure 11. Comparison of 0-d temperature scaling model for single-sided power feed, double-sided secondary configuration (Fig. 4) with the measured primary (circle) and secondary (square) radiation temperatures and pinch powers. These curves are calculated for $f_{ps} = 0.63$, $f_u = 0.8$, and $f_s = 0.10$, with the secondary entrance and AK gaps partially closed.

Figure 12. Comparison of 0-d temperature scaling model for double-sided power feed, double-sided secondary configuration (Fig. 1) and comparison with scaled Z data. The primary is 24x10 mm^2 with a single aperture. The secondary is a 17x15 mm^2 with a single aperture. The single sided Z secondary data from Fig. 10 is scaled up by $2^{1/4}$ to account for the temperature increase from an additional primary. These curves are calculated for $f_{ps} = 0.63$, $f_u = 1.0$, and $f_s = 0.10$, with the secondary entrance and AK gaps fully open.

Figure 13. 0-d energy partition of total energy between radiated and internal energy as a function of pinch current for a static, uniform W pinch column. The total energy was normalized to Z results: 1.0 MJ radiated and 0.25 MJ internal (estimate) at 19 MA load current.

Figure 14. A plot of magnetic pressure P_m from Eq. B8 (solid lines) and radiation ablation pressure P_a from Eq. B7 (dotted lines) for high-yield conditions (lines with circles) and Z conditions. The magnetic pressure exceeds the radiation ablation pressure until about 6 ns prior to stagnation.

Figure 15. Ratio of magnetic pressure to radiation ablation pressure for Z (solid line) and high yield conditions (dotted line).

Tables

Table I. Physics Issues for High Yield Assessment

Issue	Comments
Pinch energetics	scaling of pinch output with mass, current, atomic number, etc.
Power flow	radiation and current-driven closure of the magnetically-tamped power feed gap
Hohlraum energetics	relationship between x-ray power and hohlraum temperature
Radiation coupling	transport of radiation into the secondary, Be spoke transparency
Pinch power balance	power balance between the two primaries to control P1
Pinch power simultaneity	power timing between the two primaries to control P1 swing
Radiation symmetry	geometric control of even mode radiation symmetry
MHD isolation	expansion of pinch plasma into the secondary
Capsule preheat	quantify levels of plasma, high-energy particles and radiation preheat
Pulse shaping	quantify energetics, timing, and reproducibility of pulseshaping
Capsule energetics and stability	design of capsules with large radius, fuel mass and ablator energy
Capsule implosions	use capsule implosions to assess symmetry to ICF relevant levels

Table II. Definitions of Parameters in Hohlraum Equations

Parameter	Definition
P_p	pinch power
P_j	pinch power for lower or upper pinch
T_p	primary hohlraum (radiation) temperature
T_j	hohlraum (radiation) temperature for lower or upper primary
T_s	secondary hohlraum (radiation) temperature
f_p	fraction of pinch power that remains in the primary ($=1-f_s f_v f_{ps}$)
f_s	fraction of pinch power that directly shines into the secondary (viewfactor calculations: 5% to 16% depending on shine shield, secondary and pinch [Vesey *et al.* 1998; 1999])
f_{ps}	fraction of the aperture between primary and secondary that is open (prediction of 2-D RMHD calculation, $f_{ps} = 0.75$, [Hammer *et al.* 1999])
f_v	correction factor for energy loss in secondary entrance filters ($f_v = 0.9$ for 10 μm parylene filter, 1-D RMHD simulations)
f_u	ratio of upper pinch power to lower pinch power
f_p, f_s, f_{ps}, f_v	assumed to be the same for both primaries
A_{psj}	initial area of aperture between primary and secondary for each primary (cm^2)
$(1-f_{ps})A_{ps}$	fraction of area assumed to be filled with Be material (cm^2)
A_{wp}	Au wall area in primary (cm^2)
A_{wj}	Au wall area in each primary (cm^2)
A_{ws}	Au wall area in the secondary (cm^2)
A_{hp}	diagnostic aperture area in primary (cm^2)
A_{hj}	diagnostic aperture area in each primary (cm^2)
A_{hs}	diagnostic aperture area in secondary (cm^2)
A_g	area of MITL AK gap (cm^2)
A_{gu}	area of MITL AK gap feeding upper pinch if present (cm^2)
A_c	surface area of capsule (if present) (cm^2)
A_{pj}	effective loss area of each primary (cm^2)
A_s	effective loss area of the secondary (cm^2)
α_{pj}	primary wall albedo given by 1-D RMHD calculation.
α_s	secondary wall albedo given by 1-D RMHD calculation.
α_g	effective AK gap power feed albedo near peak temperature (Lightscape viewfactor calculation, $\alpha_g = 0.34$ [Vesey *et al.* 1998])
α_{gu}	effective albedo for gap feeding upper pinch in double-pinch (at peak temperature) (Lightscape viewfactor calculation, $\alpha_g = 0.40$ [Vesey *et al.* 1998])
α_{Be}	Be spoke albedo (1-D RMHD calculation, $\alpha_{Be} = 0.2$)
α_c	capsule albedo (assume, $\alpha_c \approx 0.3$ [Lindl 1995])

Figures

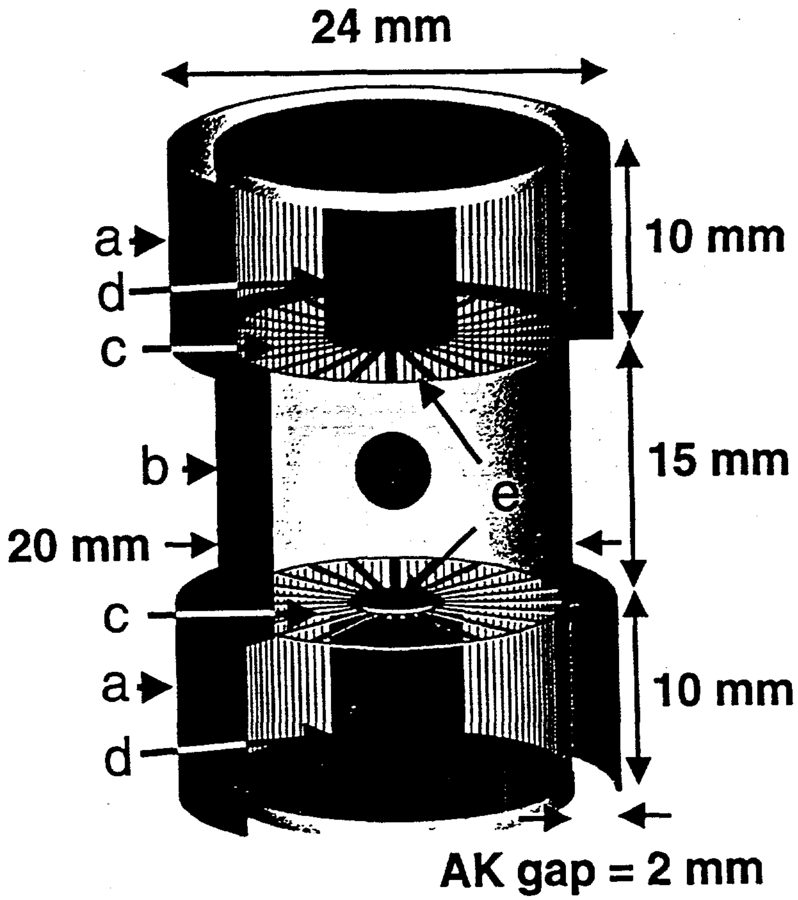

Figure 1. Cuneo et al.

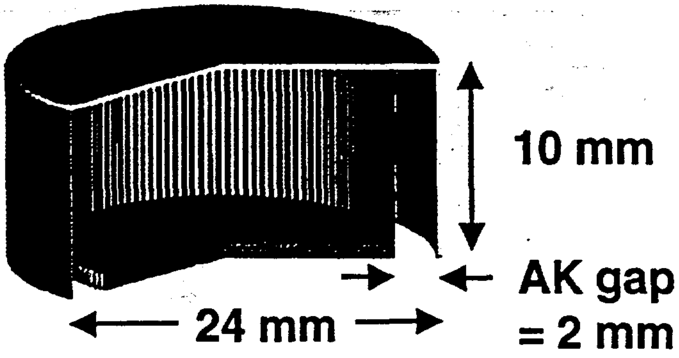

Figure 2. Cuneo et al.

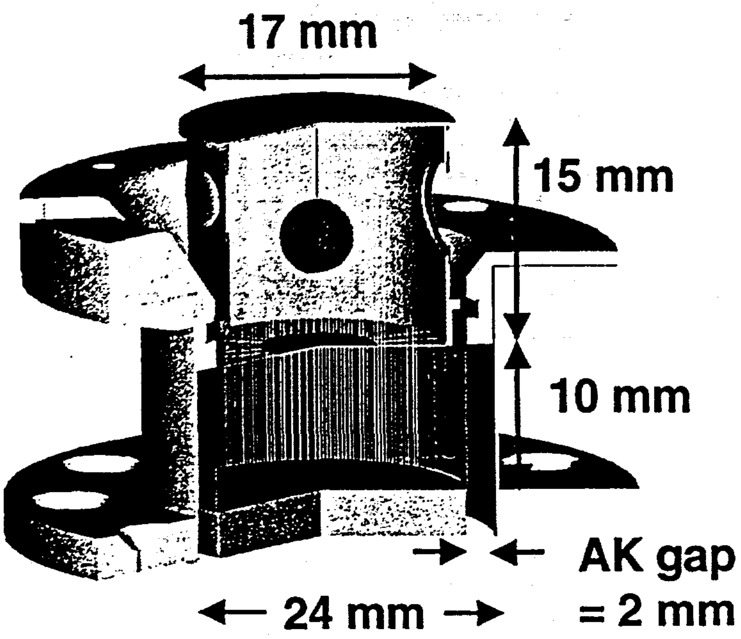

Figure 3. Cuneo et al.

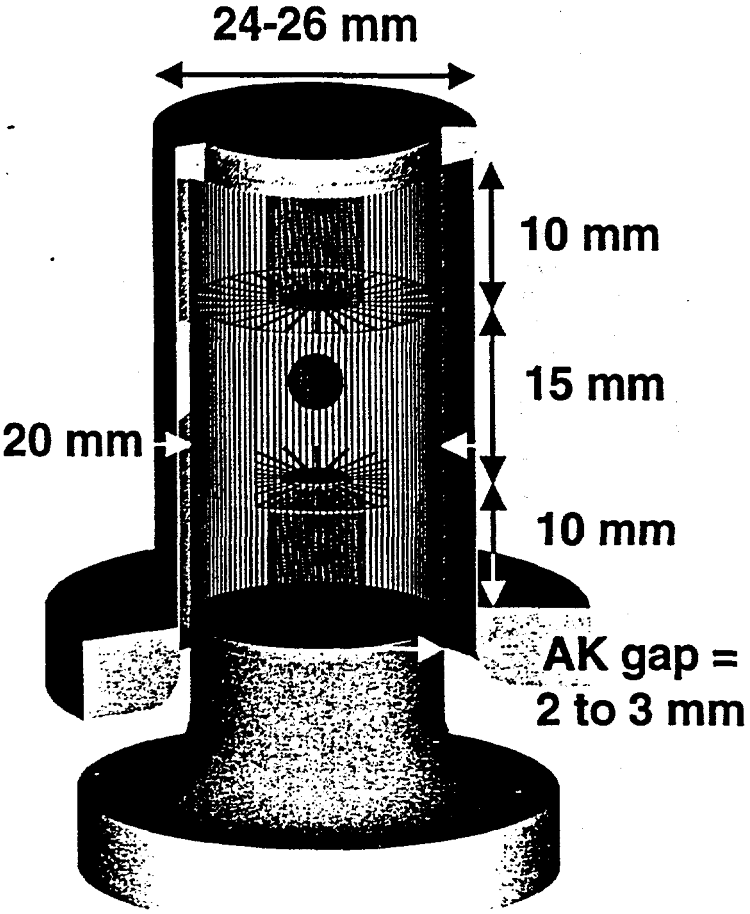

Figure 4. Cuneo et al.

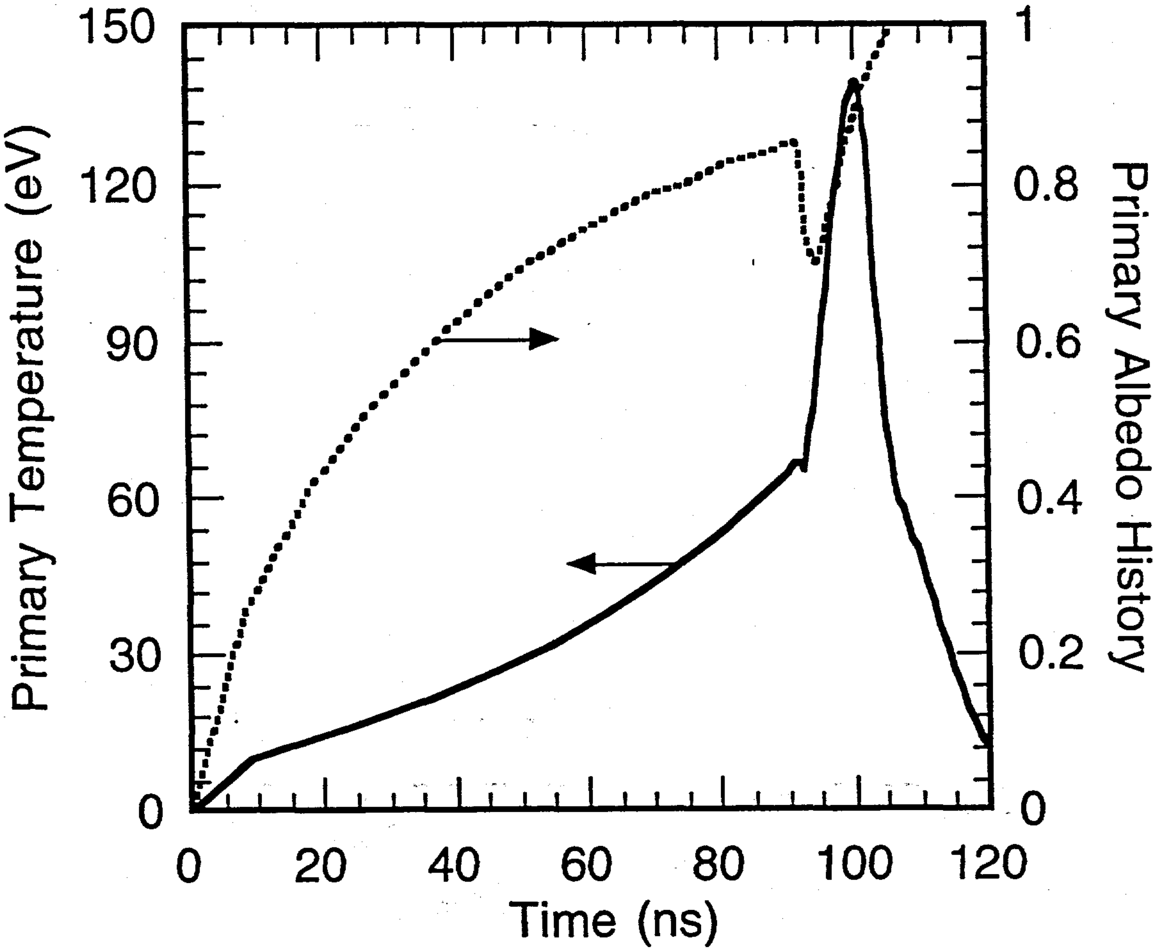

Figure 5. Cuneo et al.

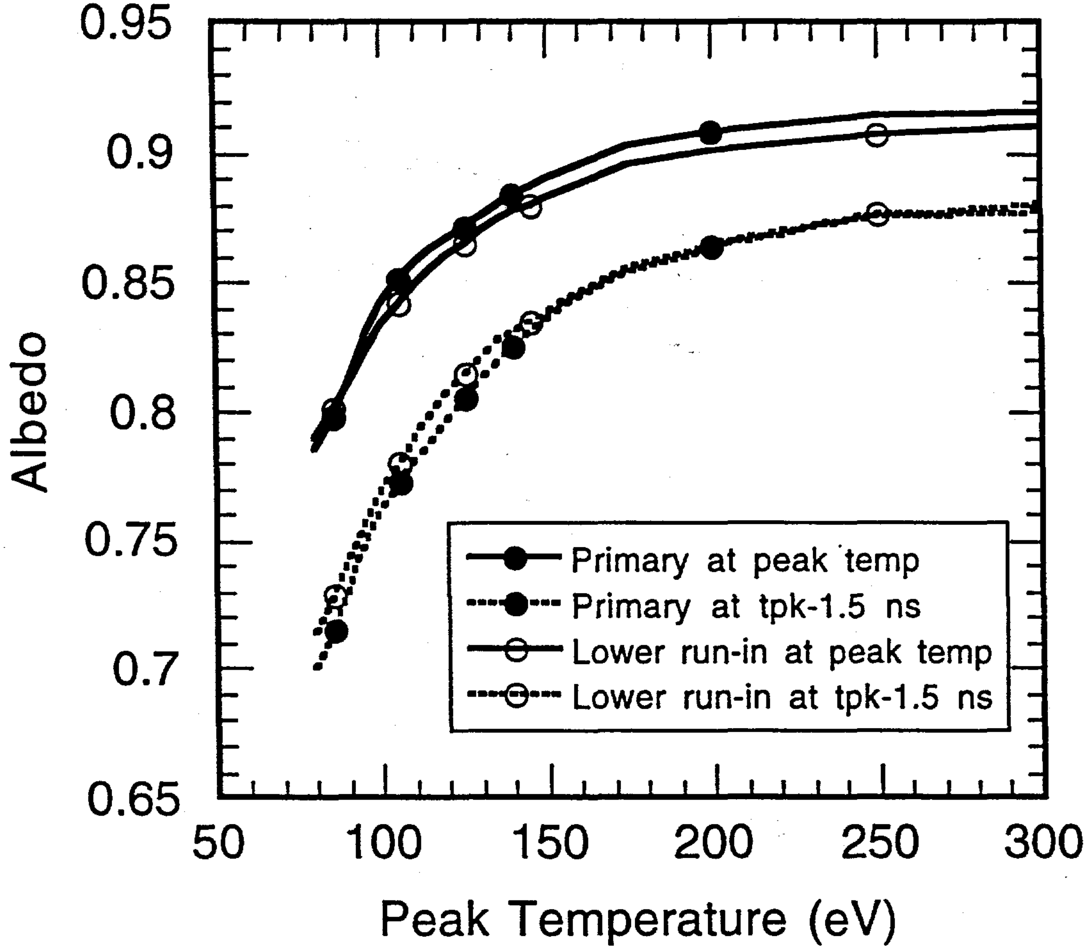

Figure 6. Cuneo et al.

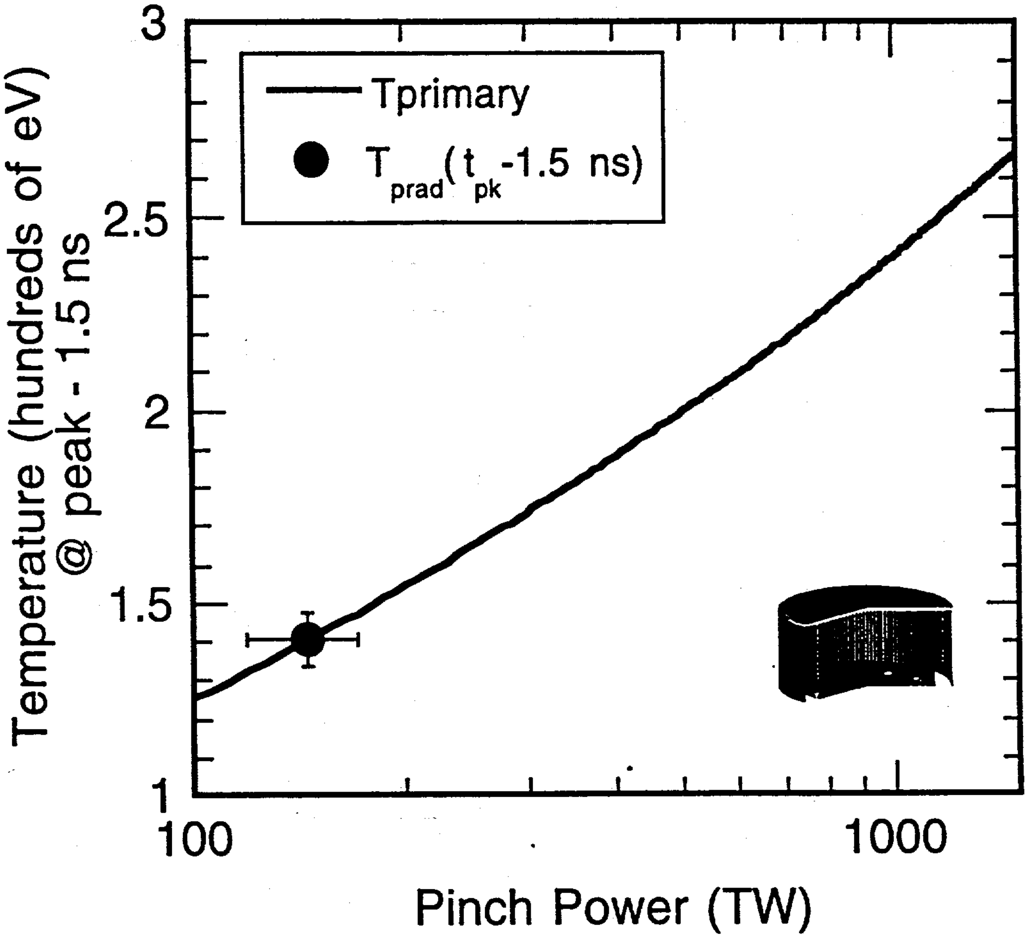

Figure 7. Cuneo et al.

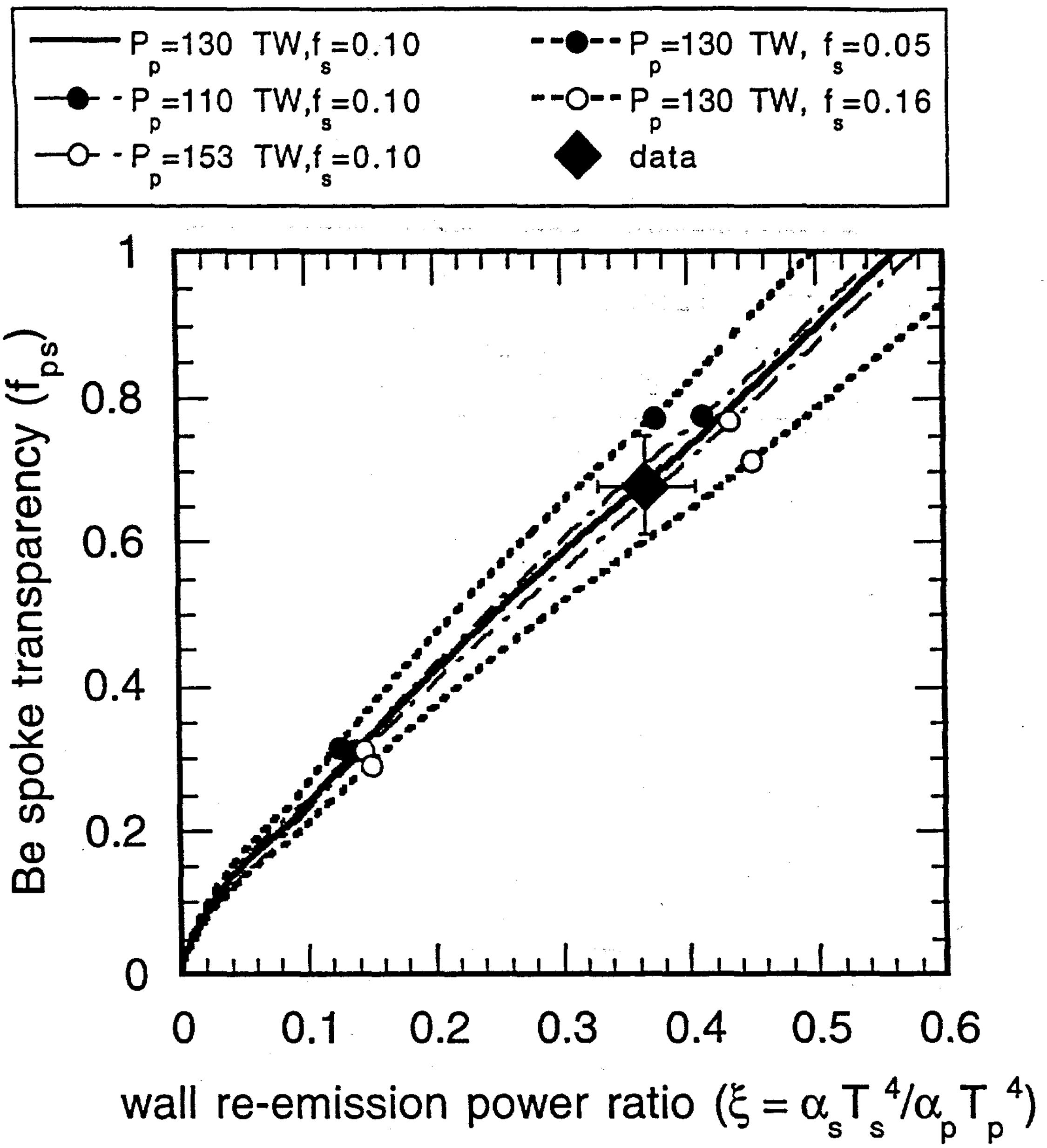

Figure 8. Cuneo et al.

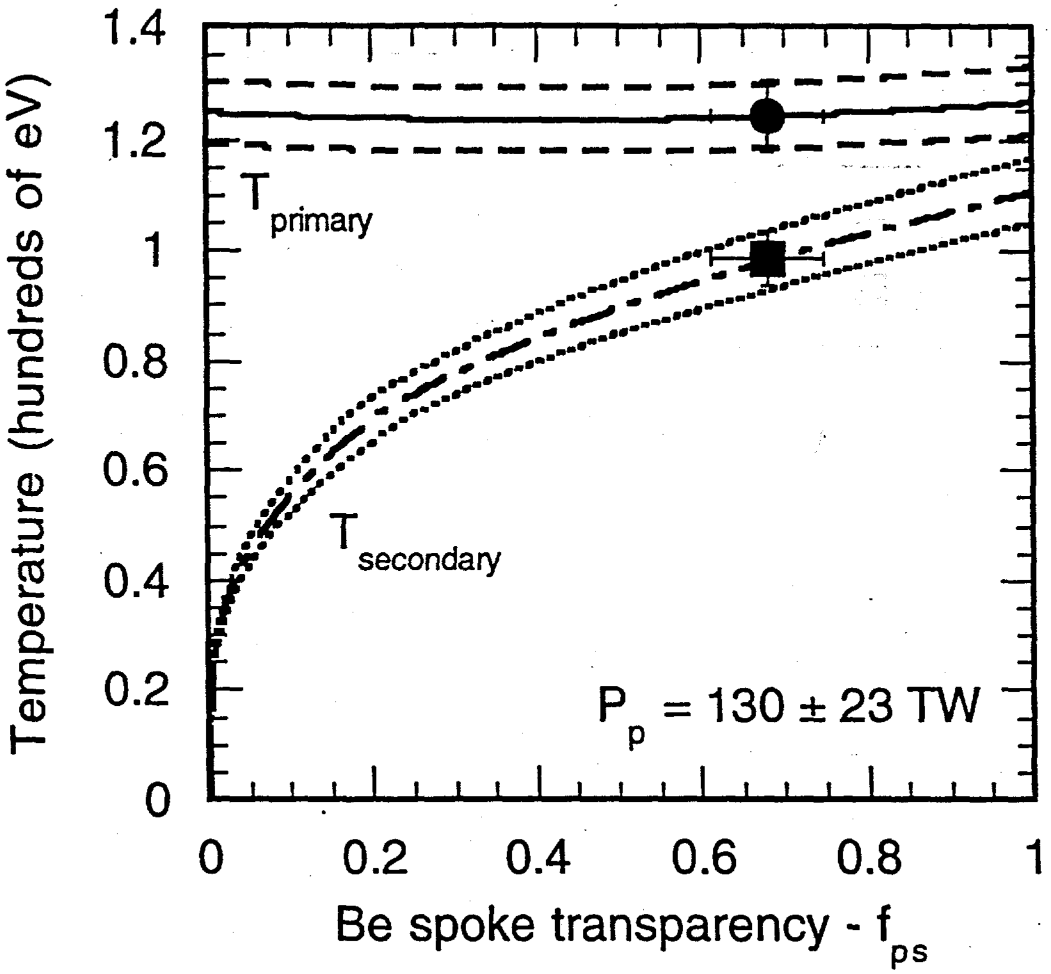

Figure 9. Cuneo et al.

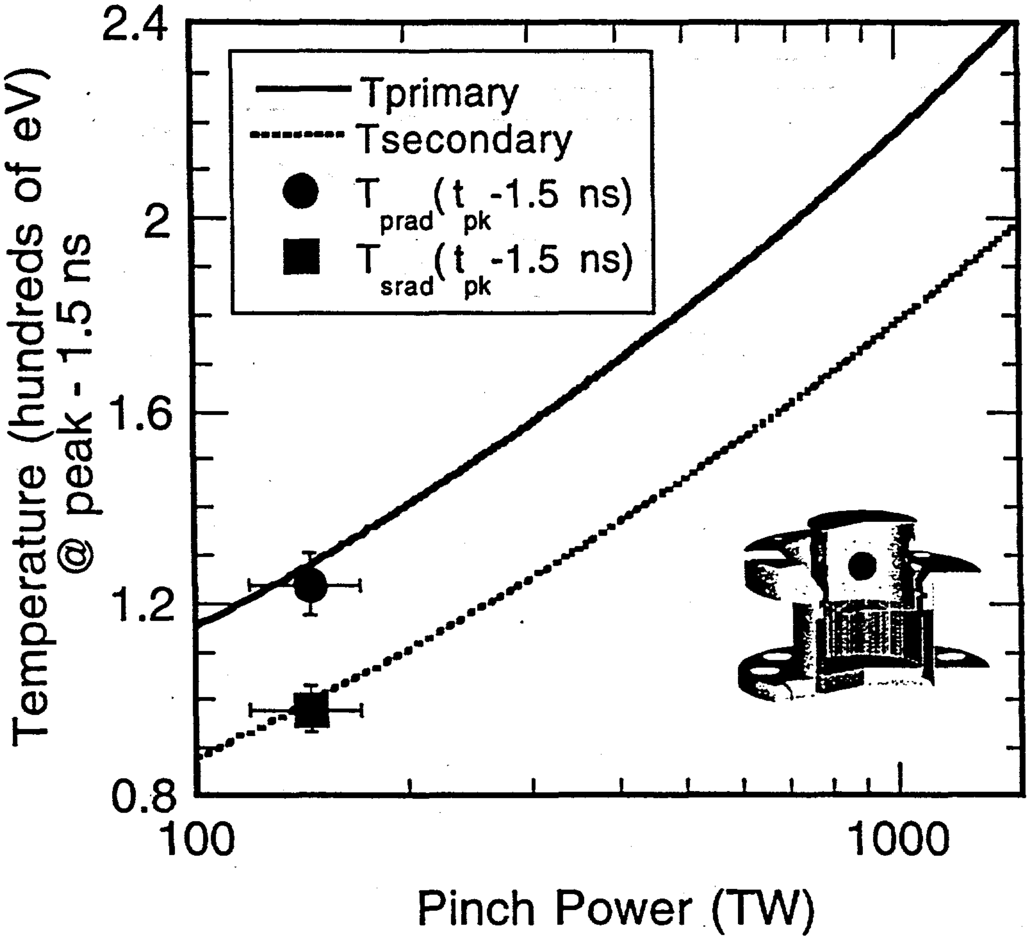

Figure 10. Cuneo et al.

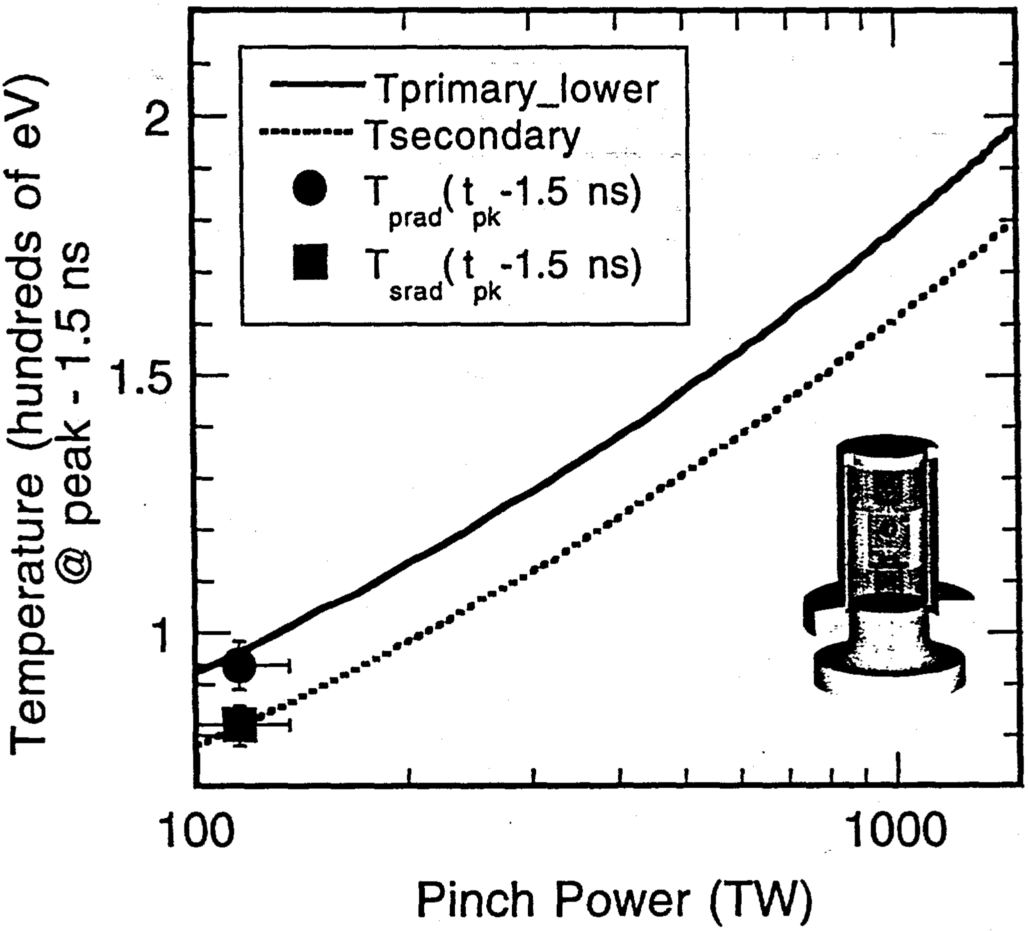

Figure 11. Cuneo et al.

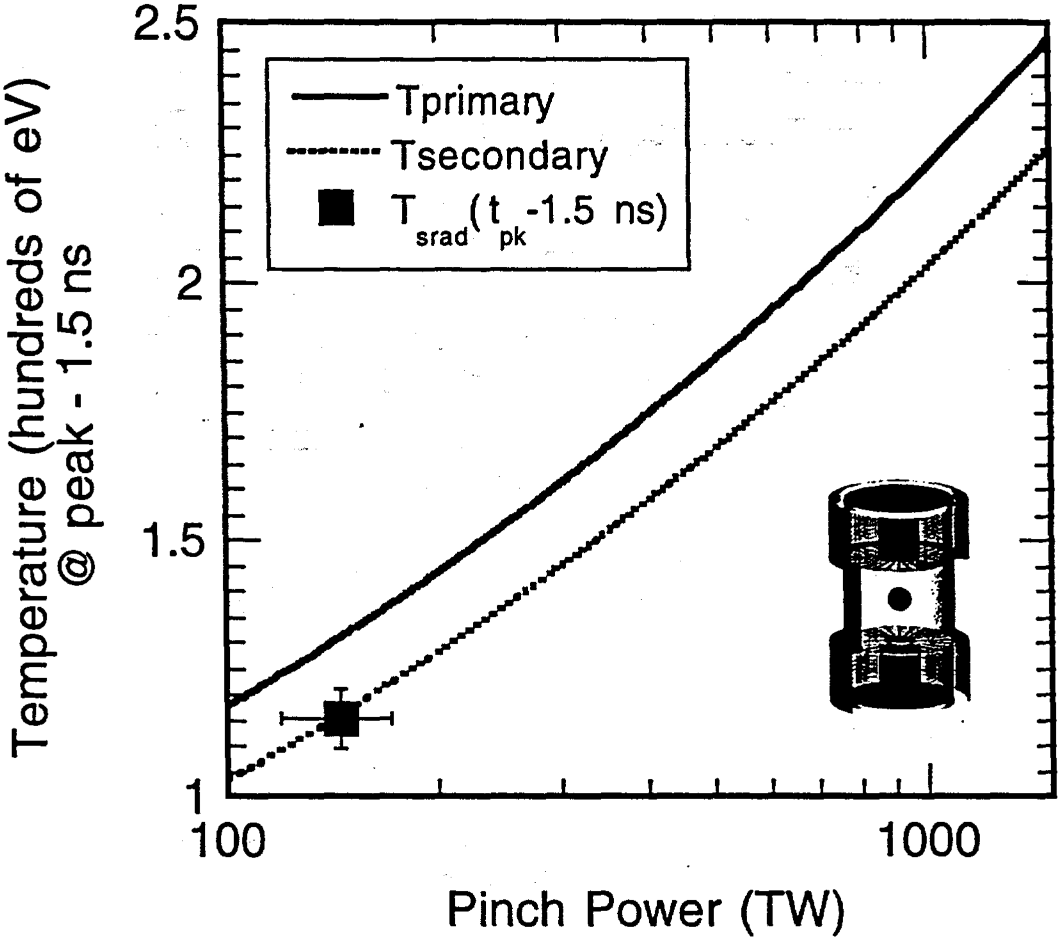

Figure 12. Cuneo et al.

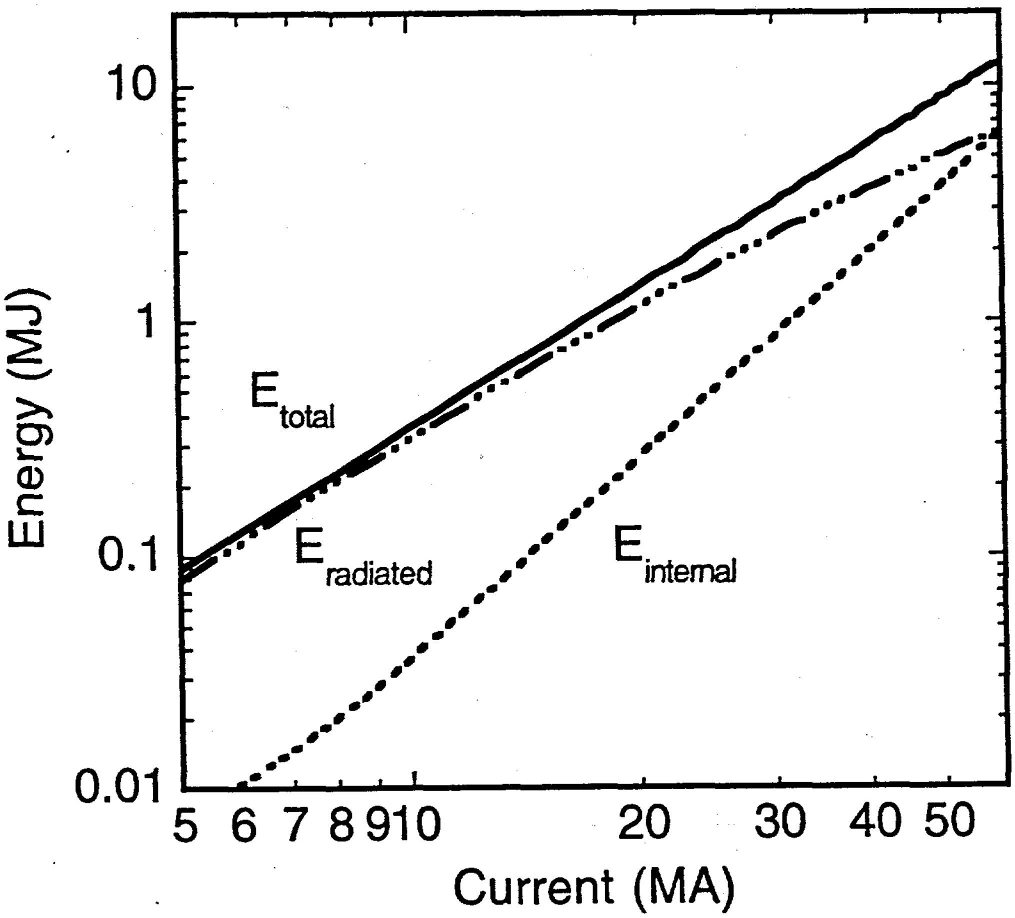

Figure 13. Cuneo et al.

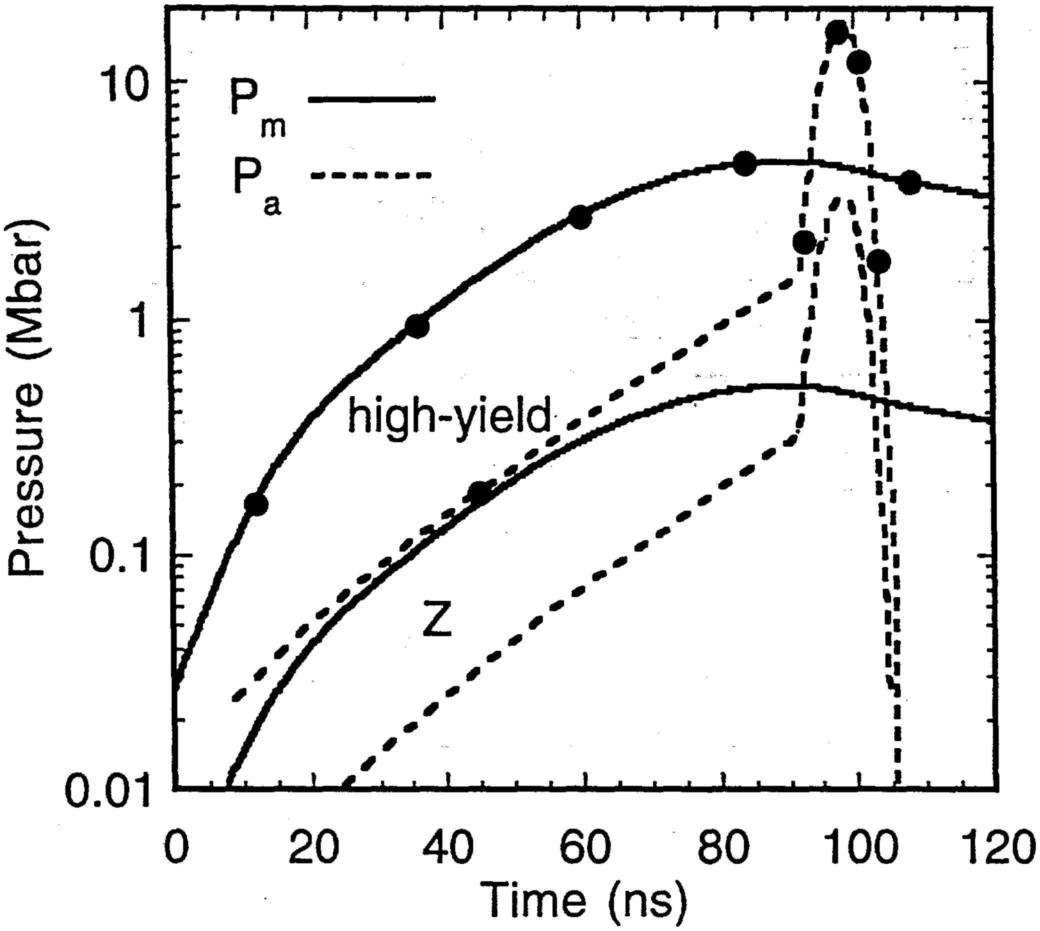

Figure 14. Cuneo et al.

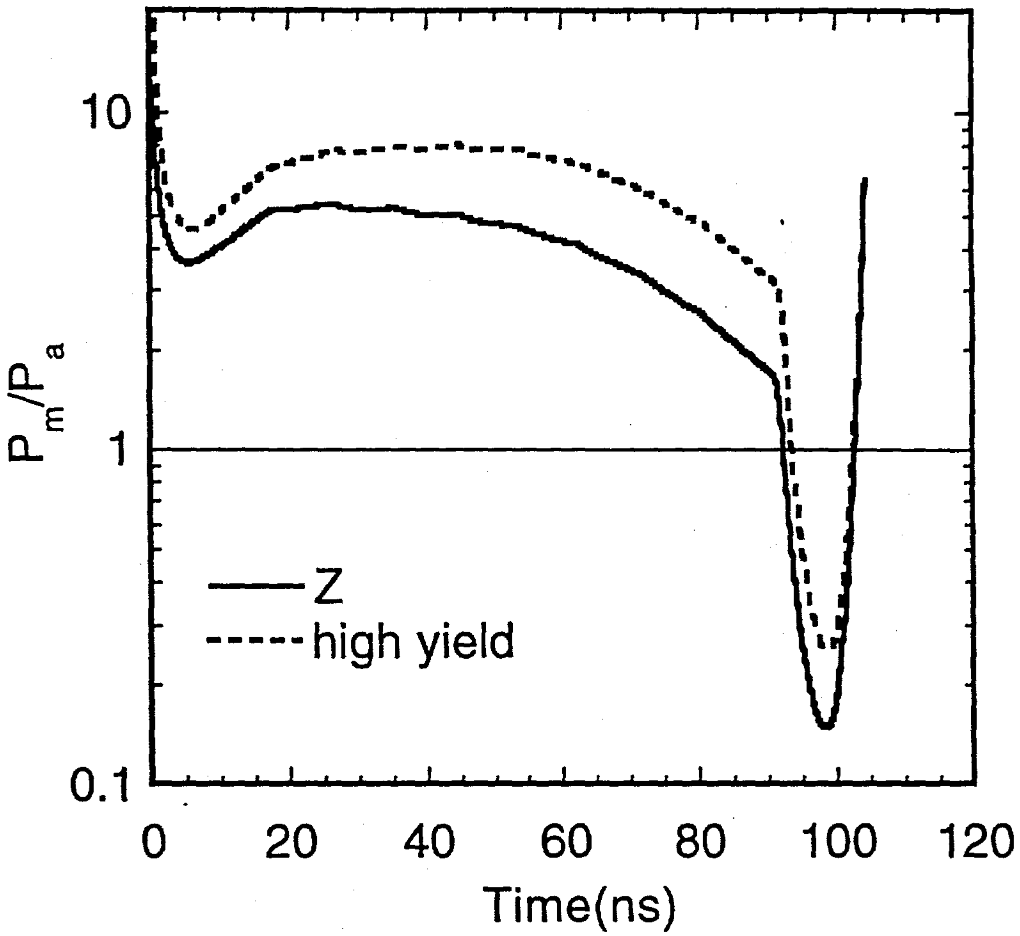

Figure 15. Cuneo et al.